Dynamic fluid simulation of hydraulic oil flow inside fatigue cracks during transient loads

Lukas Michiels*, Marcus Geimer

Institute of Mobile Machines (Mobima), Karlsruhe Institute of Technology (KIT), Karlsruhe, German, lukas.michiels@kit.edu, marcus.geimer@kit.edu

ABSTRACT

Fatigue damage plays an important role in mobile hydraulics as all components are subject to varying and highly transient loads. Transient loads lead to complex damage accumulation processes and, thereby, difficulties in design and testing. Estimation of fatigue damage during complex load cycles allows efficient design and maintenance cycles, besides being the groundwork for real-time damage monitoring in the future. The interaction between pressurized fluid and crack faces is supposed to have a significant effect on the fatigue crack growth of hydraulic components. It prevents crack closure and contact of the crack faces during unloading. In this paper, we introduce a simplified simulation for the fluid flow in narrow cracks. Coupling the fluid simulation with a mechanical solver to account for elastic pressure-related deformation is difficult in terms of numeric stability. Instead of artificially modifying the fluid properties to increase the dynamic dampening effects of the fluid, we simplify the mechanical deformation matrix and introduce damping to the mechanical deformation to improve the overall solution stability. Our results show that dynamic effects do influence the fluid flow inside cracks and, thereby, fatigue crack growth.

Keywords. Fatigue, fluid dynamics, damage accumulation, mobile hydraulics.

1. INTRODUCTION

Increasing fuel costs and the aim to reduce CO_2 emissions have driven the development of more energy-efficient hydraulic power systems in recent decades. While electrification can reduce CO_2 emissions even further, the power density of hydraulic actuators cannot be reached by electric components, [1]. For this reason, the electric hydraulic hybrid concepts are considered as alternatives to purely electric drivetrains, [2], [3], [4]. Electric and hydraulic energy storage is highly limited and improving the efficiency of all drive components is becoming even more important, [5].

Mobile machines are used in rough and challenging environments and undergo varying and highly transient loads, [6]. Due to the recurrent loading, hydraulic components are subject to wear and eventually failure when the fatigue limit is reached. Through damage accumulation, even a few events can have a negative influence on the lifetime and lead to failure before the expected life-time end, [7]. Reducing weight and improving efficiency requires knowledge of the fatigue mechanism to predict damage accumulation and define service intervals. The fatigue of hydraulic components is influenced by fluid-structure interaction (FSI). The fluid pressure represents a supplementary fatigue stress when oil is

flowing into a crack. In addition, the fluid's viscosity opposes fast volume changes and, hence, fast crack closure. In this paper, we focus on the simulation of the fluid flow inside the fatigue cracks to simulate the fluid pressure during highly transient loads. Additional fluid effects, e.g. oil wedging, need to be taken into account to calculate accurate stress amplitudes to predict fatigue damage. In the literature, several similar approaches from related fields can be found.

The experiments of Davis and Ellison, [8], showed a small decrease in crack propagation rate when submerging specimens in high viscose oil. The reduced crack propagation was explained by the decreased stress amplitude due to hydrodynamic pressure inside the crack (oil wedging). Lower crack propagation rates were also reported by [9], whereas Tzou et al., [10], reported increased crack growth for low fatigue levels of submerged specimens. Contrary to specimens in pressure-free fluids, static ambient pressure led to increased crack growth in [11].

The interaction of fluids and fatigue cracks caught the attention of researchers working on driven-over rail systems. It is assumed that fluids assist crack propagation due to surface contact pressure, [12], [13], [14]. Bower states in [12] that crack growth on rails occurs especially in combination with fluid, e.g. water, and only in the direction of movement. Two main effects are assumed to contribute to this effect. One aspect is that fluid lubricates the crack flanks, leading to increased Mode II crack growth. On the other hand, when the crack is directed in the direction of movement, the fluid is pressed into the crack and the pressure of the enclosed fluid is increasing due to the wheel's load. The additional stress is, in these cases, caused by the external wheel load and no internal oil wedging.

The Flow regime inside fatigue cracks came to attention with the "lead before break" (LBB) concept. If fatigue cracks lead to leakage of pressure reservoirs without causing rupture, fatigue damage can be sensed by the leakage. The research is mainly focused on large-scale applications in the power industry. However, similarities to hydraulic applications can be found in the leakage of pressurized cylinders, [15], [16], [17]. The experiments by Clarke et al., [15], showed a dependency of the fluid flow on the grain size. If the grain size is smaller than the crack width, a laminar flow model corresponds well, while for smaller cracks, modelling the turns and bends due to grain size is more accurate. A simplified computational fluid dynamics model was used by Bagshaw et al., [16], to simulate flow rates in narrow cracks less than 3 times the size of the surface roughness. In contrast to the presented approach, these studies focused on a constant flow through an established crack under the assumption of a constant intern load pressure of a cylinder, neglecting fluid compressibility and inertia.

The paper is structured as follows: in Section 2, a simplified fluid flow simulation is presented. In the following Section 3, the coupling of the simplified simulation with a structural simulation is described. The simplified simulation was validated based on the one-way coupled computational fluid dynamics simulation presented in Section 4. The results are discussed in Section 5, before the paper is concluded in Section 6.

2. FLUID FLOW SIMULATION

2.1. Laminar fluid model

In the following, we assume laminar flow between the crack faces. The time variable t is divided into discrete time-steps t_k with temporal resolution Δ t. The crack is subdivided into N spatial control volumes (sections), which are indicated by the incremental subscript i. The volumes are of length l_i, width b and height $h_i(\bar{p}(t))$. The height $h_i(\bar{p}(t))$ of the flow area corresponds to the mean crack opening displacement of the section. Figure 2.1 shows one section and the corresponding flow between neighboring sections. The volume flow between each section is defined as $Q_i(t)$ in the positive i direction.

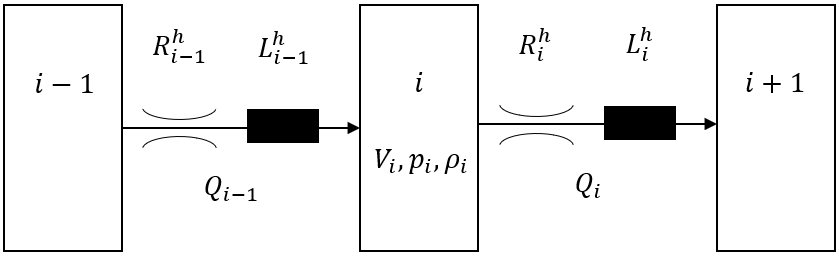

Figure 2.1. Fluid flow between discrete sections $i-1$, i, and $i+1$ with fluid volume V_i, density ρ_i, pressure p_i, and volume flow $Q_i(t)$ at section i.

The volume flow between consecutive sections is modeled using the electronic-hydraulic analogy, providing a simple and understandable dynamic model. The hydraulic flow resistance $R_i^{h(t)}$ is calculated based on the assumption of a laminar flow between two parallel plates, [18], as

$$R_i^{h(t)} = \left(12\eta \frac{l_i}{b\, h_{i(t)}^3}\right), \tag{2.1}$$

The fluid inertia of the flow between the sections i and $i+1$ characterize the hydraulic inductance $L_i^{h(t)}$ which is defined as

$$L_i^h\,(t) = \rho_i(t) \frac{l_i}{b h_i(t)}. \tag{2.2}$$

Assuming isothermal compression, the Tait equation of state is used to calculate the density for a given pressure, [19]. The bulk modulus K and the reference density ρ_0 are material constants depending on the oil. For a density exponent of $n = 1$, the density is linear proportional to the pressure change and can be calculated as

$$\rho_i(t) = \rho_0 \cdot \left(1 + \frac{p_i(t)}{K}\right). \tag{2.3}$$

Following the analogy shown in Figure 2.1, the pressure difference between sections i and $i+1$ is the total of the pressure losses at the hydraulic resistance $R_i^h(t)$ and the hydraulic inductance $L_i^h(t)$:

$$p_i(t) - p_{i+1}(t) = L_i^h(t)\frac{\delta Q_i(t)}{\delta t} + Q_i(t)R_i^h(t) \tag{2.4}$$

The pressure loss of the inductance accounts for the fluid inertia. The fluid inertia opposes fast changes in the volume flow. The time discrete solution of (2.4) for time-steps t_{k-1} and t_k is, [20],

$$\begin{aligned} Q_i(t_k) &= \widehat{Q}_i(t_k) - \left[\widehat{Q}_i(t_k) - Q_i(t_{k-1})\right]e^{-\frac{\Delta t}{\tau}} \\ &= \widehat{Q}_i(t_k)\left(1 - e^{-\frac{\Delta t}{\tau}}\right) + Q_i(t_{k-1})e^{-\frac{\Delta t}{\tau}} \end{aligned} \tag{2.5}$$

with

$$\widehat{Q}_i(t = t_k) = \frac{1}{R_i^h(t)}\left(p_i(t) - p_{i+1}(t)\right), \tag{2.6}$$

and the time factor τ_i defined as

$$\tau_i(t) = \frac{L_i^h(t)}{R_i^h(t)}. \tag{2.7}$$

The volume flow Q_{i-1} is calculated based on the fluid density ρ_{i-1} at section $i-1$. Given the conservation of mass,

$$\rho_{i-1}[Q_{i-1}]_{at\ Sec.\ i-1} = \rho_i[Q_{i-1}]_{at\ Sec.\ i}, \tag{2.8}$$

the same mass flow at section i with density ρ_i is,

$$[Q_{i-1}]_{at\ Sec.\ i} = \frac{\rho_{i-1}}{\rho_i}[Q_{i-1}]_{at\ Sec.\ i-1}. \tag{2.9}$$

In the following, Q_i is always calculated based on the density of the corresponding section i and the subscript "at Sec. i" is omitted. The volume flows at section i sum up as

$$\Delta V_i(t_k) = V_i(t_k) - V_i(t_{k-1}) = \left[\frac{\rho_{i-1}}{\rho_i}Q_{i-1}(t_k) - Q_i(t_k)\right]\Delta t. \tag{2.10}$$

The resulting pressure change dp_i is

$$\Delta p_i(t_{k+1}) = p_i(t_{k+1}) - p_i(t_k) = \frac{1}{C_i^h(t_k)}\left(\Delta V_i(t_k) - \Delta h_i(t_k)\ b\ l_i\right), \tag{2.11}$$

with the hydraulic capacity

$$C_i^h = \frac{1}{K}l \cdot h_i\left(\bar{p}(t_k)\right)b \tag{2.12}$$

The second part of (2.11) is the volume change of the section due to the motion of the crack faces $\Delta\, h_i(t_k)$:

$$\Delta h_i(t_k) = h_i\left(\bar{p}(t_k)\right) - h_i\left(\bar{p}(t_{k-1})\right). \tag{2.13}$$

A decreasing crack size $\Delta\, h_i(t_k) < 0$ is increasing the fluid pressure.

Given (2.11), the pressure at the next time-step $k+1$ is

$$p_i(t_{k+1}) = p_i(t_k) + \Delta p_i(t_k). \tag{2.14}$$

At this point, one time-step is completed, and the calculation continues with the next time-step $t = t_{k+1}$. The simulation is a pure forward model and is not iterated towards a semi-stationary steady state.

Several boundary conditions have been defined. At the last element, there is no volume flow to the next element and $Q_N(t) = 0$. The load pressure $p_0(t)$ is known for all time-steps. The simulation is initialized at time $t_0 = 0$ under the assumption of a constant pressure $p_i(t_0) \cong \sim p_0(t_0)$ throughout the crack. A structural model of the part is required to calculate the crack opening displacement $h_i\big(\bar{p}(t_k)\big)$, depending on the fluid pressure inside the crack $\bar{p}(t_k)$, the load pressure outside the crack $p_0(t)$, and any external loads.

2.2. Structural Deformation

The structural deformation can be divided into a parallel and an orthogonal component compared to the crack's orientation. The parallel component does not change the flow area inside the crack. The orthogonal component, however, changes the crack opening displacement $h_i\big(\bar{p}(t)\big)$. Under the assumption of an ideal-linear elastic material, the crack opening displacement can be defined as

$$\bar{h}\big(\bar{p}(t)\big) = \bar{h}_0\big(\bar{p}_0(t)\big) + \boldsymbol{A}\bar{p}(t) - \boldsymbol{M}\frac{\delta^2\bar{h}\big(\bar{p}(t)\big)}{\delta t^2} \tag{2.15}$$

with a stiffness matrix $\boldsymbol{A}$, an inertial matrix $\boldsymbol{M}$ and the crack opening displacement due to external loads h_0.

Both, $\boldsymbol{A}$ and $\boldsymbol{M}$ does depend on the structural surrounding of the crack but are not to be confused with the stiffness and mass matrix of the finite-element method. The stiffness matrix $\boldsymbol{A}$ can be derived from a static finite-element solution. The inertial matrix, on the other hand, is damping the structural deformation. Even as the crack closing rapidly, the structural deformation is remaining small. As $\boldsymbol{M}\,\frac{\delta^2\bar{h}(p(t))}{\delta t^2} \ll \boldsymbol{A}\,\bar{p}(t)$ the inertial dampening can be neglected. In the time-discrete simulation, an under-relaxation factor of α is used instead of the inertial matrix of $\boldsymbol{M}$ to induce inertial damping and achieve numeric stability. The crack opening displacement h_i is replaced by an under-relaxed term $\hat{h}_i$ as

$$\hat{h}_i(t_{k+1}) = \hat{h}_i(t_k) + \alpha\left[h_i\left(\bar{p}\big(t_{(k+1)}\big)\right) - \hat{h}_i(t_k)\right]. \tag{2.16}$$

The under-relaxation corresponds to a low-pass filter with smoothing factor $\alpha = \frac{\Delta t}{T_{lp}}$ with time advancement Δt and time constant T_{lp}. Hence, the time constant T_{lp} of the filter must been significantly smaller than the timescale of the expected deformations.

In the simulations, the number of sections was set to $N = 100$, the time advancement $\Delta t = 2 \cdot 10^{-9}\,s$, and the total step count to 10^7 steps. A small-time advancement was required to attain the intended accuracy. The time constant of the low-pass filter was chosen as $T_{lp} = 1 \cdot 10^{-7}\,s$ resulting in an under-relaxation factor of $\alpha = 0.02$.

3. FEM SIMULATION MODEL

The elastic deformation of the crack region is simulated with the commercial Finite-Element-Method Solver Ansys in a 3D simulation. The mesh consists of a single layer and symmetry conditions in the third direction, resulting in a quasi-2D simulation. The solid regions are meshed with hexahedron and prism elements with linear basis functions, see Figure 5.4. The base element size is 0.5 mm, being refined around the crack with an element size of 0.05 mm and 0.01 mm at the crack tip, leading to a total of approximately 28,000 elements. The material of the loaded part is modelled with a linear elastic material behavior and a Young's modulus of $E = 210\ GPa$ and a Poisson's ratio of $\nu = 0.3$.

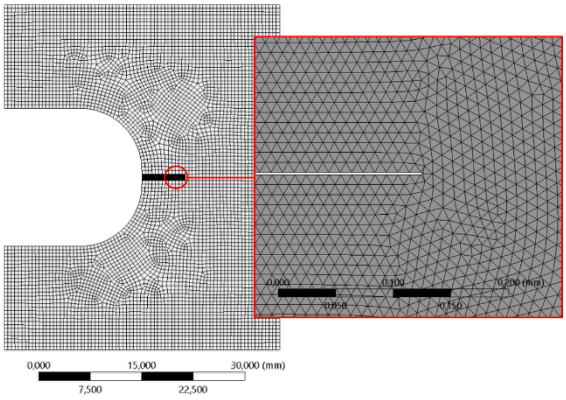

Figure 3.1. Overview of finite-element mesh and refined mesh around the crack tip

According to Section 2.1, the crack is divided into N partial subsection with a surface pressure boundary condition $\bar{p} = [p_1, \dots, p_N]$. The deformation of the crack, also referred to as crack opening displacement, is denoted as $\bar{h} = [h_1, \dots, h_N]$.

The objective of the structural analysis is to derive the stiffness matrix $\boldsymbol{A}$ of the crack region. Dividing the crack into N sections lead to a matrix $\boldsymbol{A} = [a_{i,j}]$ of shape NxN. N independent pressure distributions $\bar{p}^j$ are required to calculate the coefficients $a_{i,j}$. A lower triangular matrix with arbitrary pressure level p satisfy all required conditions:

$$\begin{aligned} \boldsymbol{P} &= [\bar{p}^1 \quad \bar{p}^2 \quad \dots \quad \bar{p}^{N-1} \quad \bar{p}^N] \\ &= \begin{bmatrix} p & p & \cdots & p & p \\ 0 & p & \dots & p & p \\ \vdots & \vdots & \ddots & \vdots & \vdots \\ 0 & 0 & \cdots & 0 & p \end{bmatrix} \end{aligned} \tag{3.1}$$

Solving the N static load cases, gives N crack deformation profiles $\boldsymbol{H}$:

$$\begin{aligned} \boldsymbol{H} &= [\bar{h}^1 \quad \bar{h}^2 \quad \dots \quad \bar{h}^{N-1} \quad \bar{h}^N] \\ &= \begin{bmatrix} \mathrm{h}_1^1 & \mathrm{h}_2^1 & \cdots & \mathrm{h}_{\mathrm{N}-1}^1 & \mathrm{h}_{\mathrm{N}}^1 \\ \mathrm{h}_1^2 & \mathrm{h}_2^2 & \dots & \mathrm{h}_{\mathrm{N}-1}^2 & \mathrm{h}_{\mathrm{N}}^2 \\ \vdots & \vdots & \ddots & \vdots & \vdots \\ \mathrm{h}_1^N & \mathrm{h}_2^N & \cdots & \mathrm{h}_{\mathrm{N}-1}^N & \mathrm{h}_{\mathrm{N}}^N \end{bmatrix} \end{aligned} \tag{3.2}$$

Following (2.15) $\boldsymbol{A}$ is calculated as

$$\boldsymbol{A} = \boldsymbol{P}^{-1}\boldsymbol{H}. \tag{3.3}$$

Additional equations are required to calculate the crack stiffness due to external loads. In this case, the load pressure is the only applied external load leading to

$$\bar{h}_0\big(p_0(t)\big) = \boldsymbol{B}p_0(t), \tag{3.4}$$

where $\boldsymbol{B}$ is an $1xN$ matrix. The FEM model with the zero-pressure loading inside the crack ($\bar{p}(t) = \bar{0}$) and the external pressure level ($p_0(t) = p^e$) as boundary conditions gives the deformation $\bar{h}^0$ due to these external loads. The linear deformation matrix $\boldsymbol{B}$ follows as:

$$\boldsymbol{B} = \frac{\bar{h}^0}{p^e} \tag{3.5}$$

4. COUPLED FLUID SIMULATION

Since experimental studies of the fluid flow inside fatigue cracks are difficult, the simplified simulation described in Section 2.1 was compared to a CFD analysis. For the analysis, the commercial CFD software Ansys Fluent was used. Table 4.1 gives an overview of the analysis's parameters.

The fluent area was meshed with hexahedron elements with $N = 100$ elements in the direction of the crack and 20 elements in the orthogonal direction. In the third direction, only one element with symmetric boundary conditions was used, resulting in a quasi-2D simulation. The boundary conditions were a pressure inlet at the crack mouth and the symmetry conditions in the z-direction. The inlet pressure corresponded to the external load pressure.

Table 4.1. Summary of CFD analysis

Program	Ansys Fluent 2020R2
Solver	Coupled
Base Function	Quadratic
Number of elements	2000
Boundary conditions	Pressure inlet, Grid Motion
Time-Steps	1000 à 0.02 ms

The wall motion of the crack faces was modelled as an additional boundary condition. The crack deformation was precalculated using the simplified simulation described in Section 2.1 and was imposed as a boundary condition to the simulation. Before the simulation, a DEFINE_GRID_MOTION function for Ansys Fluent was written in a UDF file defining the wall motion, and the mesh was updated at every time-step to account for the wall motion. Therefore, the CFD-Simulation was one-way coupled to the structural analysis. A direct coupling of the CFD simulation with the structural analysis is difficult in terms of stability and greatly increases simulation time.

The CFD simulation was only used for validation. If the assumption of a laminar flow between two parallel plates holds true, the simulated pressure inside the crack should be identical to the pressure simulated by the CFD simulation. The volume flow is imposed by

the wall motion and the compressibility of the fluid and is therefore identical in both analyses.

In addition to the wall motion due to the structural deformation, the mesh was pre-deformed to simulate bent cracks. Each node was randomly displaced orthogonal to the crack's direction, leading to a more realistic crack structure. Figure 4.1 depicts the crack structure for a mean nodal displacement of 20 μm. The nodal displacement could be compared to a possible grain structure. The simplified simulation accounts for the nodal displacement by increasing the section length l_i to correspond to the effective crack length.

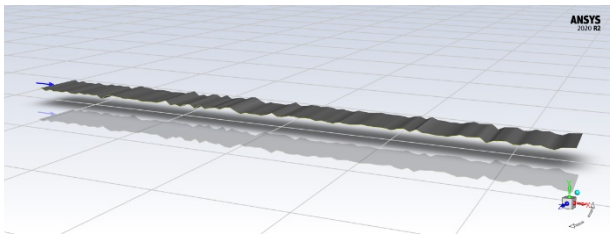

Figure 4.1. Crack structure with a mean nodal displacement of 20 μm and pressure inlet on the left side.

5. RESULTS AND DISCUSSION

5.1. Setup

The simplified simulation was used in the following to simulate the fluid flow and the structural deformation during a single pressure pulse. The load pressure was defined as a time sequence based on the pressure rise rate (positive temporal pressure gradient), the upper-pressure level, and the pressure drop rate (negative temporal pressure gradient). A rise rate of $\Delta p_r = 100\ kbar/s$ and an upper pressure level $p_{max} = 300\ bar$ were used for all simulations. The hold time of the upper and lower pressure resulted from the overall pulse length of one pulse of $t = 0.02\ s$. The used pulse length results in a pulse frequency of $f = 50hz$ which is significantly faster than current pulse experiments. However, in each pulse, the crack is filled with oil, and therefore, an increased pulse length would not change the results. In comparison with a two-way coupled fluid-structure interaction simulation, the simplified simulation significantly decreases simulation time. The total amount of 10^7 time-steps were solved on an AMD Epyc Rome server system in about 5 to 10 minutes. Three drop rates were compared in the simulations, $\Delta p_d = 50, 250, 300\ kbar/s$.

5.2. Results

Oil wedging occurs when oil is trapped inside a crack due to its high flow resistance. The magnitude of this effect increases with high pressure drop rates. Figure 5.1a shows the absolute crack tip pressure in dependence of the drop rate. For pressure drop rates lower than $50\ kbar/s$ oil wedging was not significant, and the crack tip pressure did not exceed the load pressure. In the case of high pressure drop rates, however, the crack tip pressure did exceed the load pressure by a factor of up to three. This high pressure was located at the crack tip after the release of the load pressure and decreased with time, see Figure 5.2.

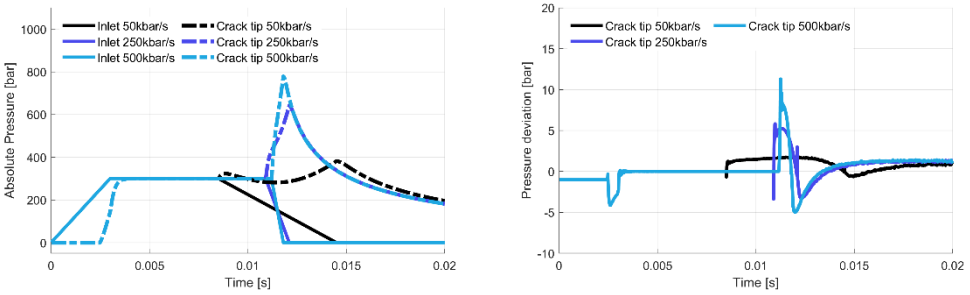

a) Simulated crack tip pressure.

b) Crack tip pressure deviation compared to non-simplified CFD.

Figure 5.1. Crack tip pressure of the FSI-simulation over one pulse at drop rates of $50, 250,$ and $500\ kbar/s$ with a nominal load pressure of $300\ bar$.

The results of the simplified simulation were compared to the results of the CFD simulation for validation. In the case of a straight crack, the simulated pressure corresponded well to the CFD simulation, as can be seen in Figure 5.1b. Contrary to the simplified simulation, the CFD simulation accounts for fluid flow orthogonal to the crack. The orthogonal component (y-direction) of the velocity, however, remains insignificantly small inside the crack, and therefore, neglecting it does not significantly change the overall fluid flow. The existing deviations could be explained by the spatial and temporal discretization and numeric effects.

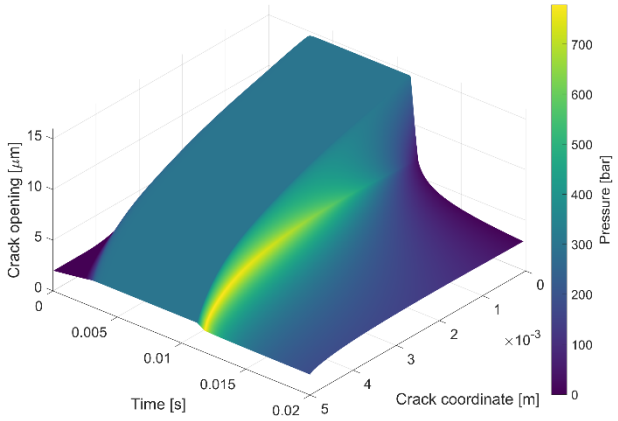

Figure 5.2. Pressure distribution and crack opening displacement during one pulse at a drop rate of $500\ kbar/s$ and a load pressure of $300\ bar$.

The focus on the electronic-hydraulic analogy was motivated by a simple integration of fluid inertia and compressibility. In Figure 5.3a the minimal and maximal density inside the crack is shown. As the crack opened, cavitation inside the crack occurred, and gaseous liquid fluid was inside the crack. As the crack closed, the fluid was compressed by the closing crack. Fluid pressure and density increased significantly. The compressibility of the oil was opposed to the increasing pressure, leading to lower pressure levels inside the crack.

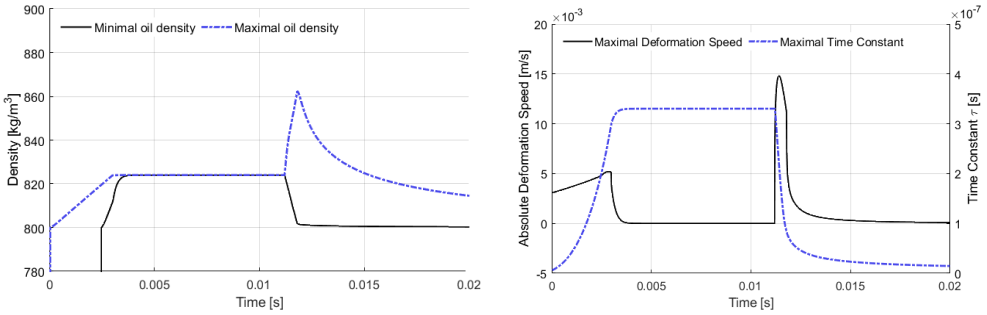

a) Minimal and maximal oil density (isothermal compression).

b) Structural deformation speed and electronic-hydraulic time constant.

Figure 5.3. Compression and dynamic properties of the simulated crack at a drop rate of 500 $kbar/s$ and a load pressure of 300 bar.

In contrast to the pressure, the fluid inertia did not play a significant role. In Figure 5.3b, the time factor and the structural deformation speed are shown. The time factor ($\tau \approx 0.35\ \mu s$) is small in comparison to the simulation timescale ($t = 0.02\ s$). The same holds true for the inertia of the structure. While the deformation occurred in a short time ($t = 0.02\ s$), it's magnitude ($\Delta h \approx 5 - 10\ \mu m$) was significantly smaller. As a result, the deformation speed remained low ($v_{def} < 0.015\ \frac{m}{s}$), and the inertia can be neglected.

The pressure inside the crack increased with the nodal displacement of the crack mesh, see Figure 5.4. This pressure increase can be explained by the increasing effective crack length and the decreasing flow area. On the other hand, the accuracy of the simplified simulation decreases as the discrepancy between the theoretic background of parallel plates and the crack geometry increases.

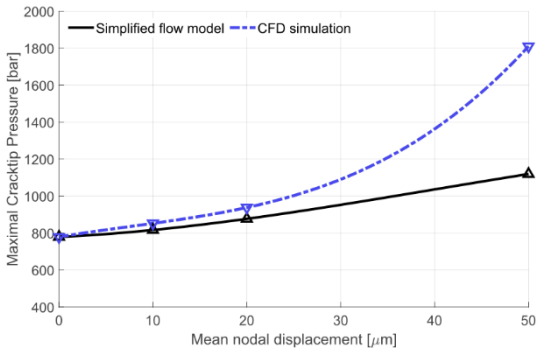

Figure 5.4. Crack tip pressure in relation to the mean nodal displacement of the mesh. The simplified simulation (black) is compared to the CFD simulation (blue). At a drop rate of 500 $kbar/s$ and a load pressure of 300 bar.

6. CONCLUSION

Fluid flow inside fatigue cracks is changing the fatigue properties of hydraulic power systems. Ignoring the fluid inside the crack leads to an underestimation of the fatigue stress. On the other hand, fluid flow properties, especially the fluid's flow resistance, lead to superposed impacts like oil wedging that reduce the effective stress amplitude. Accurate simulations of the fluid pressure and the crack displacement are required to determine stress amplitudes and fatigue crack growth.

In this paper, we developed a simplified simulation, assuming laminar flow, to simulate fluid flow inside fatigue cracks of hydraulic components. The electronic-hydraulic analogy allows one to derive a laminar flow model which accounts for fluid compressibility and inertia. The simplifications lead to a significant reduction in computational time compared to two-way coupled fluid-structure interaction simulations.

The results show that the assumption of laminar flow between two parallel plates holds true for straight cracks. A more complex crack geometry with turns and bends, e.g. caused by grain boundaries, has been simulated by a nodal displacement of the fluid mesh. In these cases, the simplified flow simulation does not lead to identical results, and the deviations increase with higher distortion. The simulations showed that the fluid inside the crack has a significant influence on the crack opening displacement and, therefore, on the resulting fatigue stress.

Besides, the distortion of the crack is modelled as a smooth wall. In future work, crack geometries should be measured in experiments and integrated into the fluid simulation. Direct validation of the fluid flow inside the crack is difficult due to the crack's dimensions. Experiments could be performed and compared to the simulations in terms of deformation and fatigue crack propagation. Additionally, the structural analysis could be extended to account for non-linear plastic deformation at the crack tip.

7. REFERENCES

[1] Y. Tanaka, S. Sakama, K. Nakano, and H. Kosodo, “Comparative Study on Dynamic Characteristics of Hydraulic, Pneumatic and Electric Motors,” in *ASME/BATH 2013 Symposium on Fluid Power and Motion Control*, Sarasota, Florida, USA: American Society of Mechanical Engineers, Oct. 2013. doi: 10.1115/FPMC2013-4459.

[2] K.-E. Rydberg, “Energy Efficient Hydraulic Hybrid Drives,” presented at the 11:th Scandinavian International Conference on Fluid Power, SICFP’09, June 2-4, Linköping, Sweden, 2009.

[3] G. Niu, F. Shang, M. Krishnamurthy, and J. M. Garcia, “Design and Analysis of an Electric Hydraulic Hybrid Powertrain in Electric Vehicles,” *IEEE Transactions on Transportation Electrification*, vol. 3, no. 1, pp. 48–57, Mar. 2017, doi: 10.1109/TTE.2016.2628792.

[4] A. Lajunen, P. Sainio, L. Laurila, J. Pippuri-Mäkeläinen, and K. Tammi, “Overview of Powertrain Electrification and Future Scenarios for Non-Road Mobile Machinery,” *Energies*, vol. 11, no. 5, Art. no. 5, May 2018, doi: 10.3390/en11051184.

[5] S. Hui, Y. Lifu, and J. Junqing, “Hydraulic/electric synergy system (HESS) design for heavy hybrid vehicles,” *Energy*, vol. 35, no. 12, pp. 5328–5335, Dec. 2010, doi: 10.1016/j.energy.2010.07.027.

[6] L. Brinkschulte, *Assistenzsysteme zur Reduktion des Schädigungsverhaltens von Komponenten einer mobilen Arbeitsmaschine*, vol. 90. Karlsruhe: KIT Scientific Publishing, 2021. doi: 10.5445/KSP/1000130176.

[7] S. K. Paul and S. Tarafder, “Cyclic plastic deformation response at fatigue crack tips,” *International Journal of Pressure Vessels and Piping*, vol. 101, pp. 81–90, Jan. 2013, doi: 10.1016/j.ijpvp.2012.10.007.

[8] F. H. Davis, E. G. Ellison, and W. J. Plumbridge, “Effects of Hydrostatic Pressure on the Rate of Fatigue Crack Growth,” *Fatigue & Fracture of Engineering Materials & Structures*, vol. 12, no. 6, pp. 511–525, 1989, doi: https://doi.org/10.1111/j.1460-2695.1989.tb00560.x.

[9] C. J. Polk, W. R. Murphy, and C. N. Rowe, “Determining Fatigue Crack Propagation Rates in Lubricating Environments through the Application of a Fracture Mechanics Technique,” *A S L E Transactions*, vol. 18, no. 4, pp. 290–298, Jan. 1975, doi: 10.1080/05698197508982771.

[10] J.-L. Tzou, S. Suresh, and R. O. Ritchie, “Fatigue crack propagation in viscous environments,” in *Mechanical Behaviour of Materials*, J. CARLSSON and N. G. OHLSON, Eds., Pergamon, 1984, pp. 711–717. doi: 10.1016/B978-1-4832-8372-2.50090-7.

[11] W. J. Plumbridge, P. J. Ross, and J. S. C. Parry, “Fatigue crack growth in liquids under pressure,” *Materials Science and Engineering*, vol. 68, no. 2, pp. 219–232, Jan. 1985, doi: 10.1016/0025-5416(85)90411-2.

[12] A. F. Bower, “The Influence of Crack Face Friction and Trapped Fluid on Surface Initiated Rolling Contact Fatigue Cracks,” *Journal of Tribology*, vol. 110, no. 4, pp. 704–711, Oct. 1988, doi: 10.1115/1.3261717.

[13] M. Akama and T. Mori, “Boundary Element Analysis of Effects of Crack Face Friction and Trapped Fluid on Rolling Contact Fatigue Cracks,” *QR of RTRI*, vol. 46, no. 4, pp. 231–237, 2005, doi: 10.2219/rtriqr.46.231.

[14] D. I. Fletcher, P. Hyde, and A. Kapoor, “Modelling and full-scale trials to investigate fluid pressurisation of rolling contact fatigue cracks,” *Wear*, vol. 265, no. 9, pp. 1317–1324, Oct. 2008, doi: 10.1016/j.wear.2008.02.025.

[15] L. V. Clarke, H. Bainbridge, S. B. M. Beck, and J. R. Yates, “Measurement of fluid flow rates through cracks,” *International Journal of Pressure Vessels and Piping*, vol. 71, no. 1, pp. 71–75, Apr. 1997, doi: 10.1016/S0308-0161(96)00056-7.

[16] N. M. Bagshaw, S. B. M. Beck, and J. R. Yates, “Identification of fluid flow regimes in narrow cracks,” *Proceedings of the Institution of Mechanical Engineers, Part C: Journal of Mechanical Engineering Science*, vol. 214, no. 8, pp. 1099–1106, Aug. 2000, doi: 10.1243/0954406001523542.

[17] C. Hong, Y. Asako, and J.-H. Lee, “Estimation of Leak Flow Rates Through Narrow Cracks,” *Journal of Pressure Vessel Technology*, vol. 131, no. 5, Sep. 2009, doi: 10.1115/1.3147984.

[18] B. S. Massey, *Mechanics of fluids*. Van Nostrand Reinhold, 1989.

[19] G. A. Neece and D. R. Squire, “Tait and related empirical equations of state,” *J. Phys. Chem.*, vol. 72, no. 1, pp. 128–136, Jan. 1968, doi: 10.1021/j100847a024.

[20] S. H. Russ, “Circuit Elements: Resistance, Capacitance, and Inductance,” in *Signal Integrity: Applied Electromagnetics and Professional Practice*, S. H. Russ, Ed., Cham: Springer International Publishing, 2022, pp. 43–63. doi: 10.1007/978-3-030-86927-4_4.

Biographies

Lukas Michiels studied mechanical engineering at the Karlsruhe Institute of Technology and the Institut national des sciences appliquées de Lyon, with a focus on robotics and computer science. Since 2021, he is a PhD student at the institute for mobile machinery at KIT, focusing on the fluid simulation in the context of hydraulic drives of mobile machines.